Evidence of three-nucleon force effects from 130 MeV deuteron-proton breakup cross section measurement

St. Kistryn,[1,*] A. Micherdzińska,[2] R. Bieber,[3] A. Biegun,[2] K. Bodek,[1] K. Ermisch,[3] W. Glöckle,[4] J. Golak,[1] N. Kalantar-Nayestanaki,[3] H. Kamada,[5] M. Kiš,[3] A. Kozela,[6] J. Kuroś-Żołnierczuk,[1,†] A. Nogga,[7] M. Mahjour-Shafiei,[3] R. Skibiński,[1] E. Stephan,[2] H. Witała,[1] J. Zejma,[1] and W. Zipper[2]

[1]*Institute of Physics, Jagellonian University, PL-30059 Kraków, Poland*

[2]*Institute of Physics, University of Silesia, PL-40007 Katowice, Poland*

[3]*Kernfysisch Versneller Instituut, NL-9747 AA Groningen, The Netherlands*

[4]*Institut für Theoretische Physik II, Ruhr Universität Bochum, D-44780 Bochum, Germany*

[5]*Department of Physics, Kyushu Institute of Technology, 1-1 Sensucho, Tobata, Kitakyushu 804-8550, Japan*

[6]*Institute of Nuclear Physics, PL-31342 Kraków, Poland*

[7]*Department of Physics, University of Arizona, Tucson, Arizona 85721, USA*

(Received 17 June 2003; published 25 November 2003)

The measurement of exclusive deuteron-proton breakup for kinematics covering a large fraction of the available phase space has been performed using 130 MeV deuteron beam. High precision fivefold cross section data in 38 kinematical configurations have been compared to predictions of modern nuclear forces. To this aim the three-nucleon (3*N*) Faddeev equations have been solved rigorously using the nucleon-nucleon (*NN*) potentials AV18, charge-dependent Bonn, Nijm I, and Nijm II alone, and combining them with the 2π-exchange Tucson-Melbourne three-nucleon force (TM 3NF) and with its modified version TM99, more consistent with chiral symmetry. The AV18 potential was also combined with the Urbana IX 3NF. Global comparison of the measured cross sections to pairwise *NN* force predictions only and with 3NF's included clearly reveals the presence of 3NF effects. Our study demonstrates the usefulness of the kinematically complete breakup reaction studied in the full phase space to search for 3NF effects.

DOI: 10.1103/PhysRevC.68.054004 PACS number(s): 21.30.−x, 21.45.+v, 25.10.+s, 24.70.+s

I. INTRODUCTION

The nucleon-induced deuteron breakup reaction has been considered for long as a valuable tool to test the three-nucleon (3*N*) Hamiltonian. In particular, it was hoped that studying this reaction will reveal the importance and structure of a three-nucleon force (3NF) in the potential energy of the 3*N* system [1,2]. Until recently, two obstacles prevented the successful use of the breakup process in such studies. The first was connected with the difficulties in solving rigorously 3*N* equations in the continuum for realistic forces, which prohibited clear statements in such a study. The rapid progress in supercomputer technology has made it now possible to gain numerically exact solutions of the 3*N* Faddeev equations for any nucleon-nucleon (*NN*) interaction, even with the inclusion of a 3NF [3]. The second obstacle was (and is) due to difficulties in performing kinematically complete, high-precision breakup measurements.

The main part of the potential energy of three interacting nucleons comes from pairwise forces. Present day models of *NN* interactions, mostly phenomenological and/or based on a meson-exchange picture, have achieved a high degree of maturity. It was possible, by adjusting model parameters, to describe *NN* data with high precision (χ^2/data-point$\approx$1) in the large energy range from threshold to about 350 MeV [7,4–6]. These so called realistic potentials, AV18 [4], charge-dependent (CD) Bonn [5,6], and Nijm I and II [7], are now extensively used in few-nucleon studies. Recent developments of chiral perturbation theory (ChPT) lead to *NN* potentials, where the multipion exchange is treated unambiguously according to chiral symmetry [8–15]. In this way the theoretical uncertainties of meson-exchange based models at long range have been mostly removed and the theory of nuclear forces is set up on a more solid and systematic basis. First calculations within the ChPT framework are quite successful in describing the data for 3*N* and 4*N* systems [16–21]. In this investigation, however, we restrict ourselves to still use only the above mentioned realistic *NN* potentials.

The present state of realistic *NN* potential models, all describing *NN* data with high precision and essentially equally good, allows one, when going to more than 2*N* systems, to concentrate on the significance and properties of many-body force contributions to the nuclear Hamiltonian. We define them as deviations of the 3*N*-system data from *NN*-force-only predictions. In case of three nucleons, the first indication on the importance of 3NF contributions came from ^{3}He and ^{3}H bound state studies. All realistic *NN* potentials are unable to reproduce their experimental binding energies, leading to underbinding in ^{3}He and ^{3}H of the order of 0.5–1 MeV [22]. This clear cut underbinding exists also for ^{4}He, where it amounts to 2–4 MeV [22–24]. Also for higher mass nuclei, where stochastic techniques must be applied, realistic *NN* forces failed to provide the experimental binding energies [25–29].

*Electronic address: skistryn@if.uj.edu.pl

†Present address: Nuclear Theory Center, Indiana University, Bloomington, IN 47405.

A natural step to explain these underbindings was to consider 3NF's in the nuclear Hamiltonian. Presently, the most often used dynamical process is the 2π exchange between three nucleons. An important dynamical ingredient in that process is the intermediate excited nucleon state Δ, as initiated long time ago by the Fujita-Miyazawa 3NF [30]. It was augmented later by further ingredients leading to the Urbana IX [31] and Tucson-Melbourne (TM) [32] 3NF's, which are mostly used in present day few-nucleon calculations. By properly adjusting the parameters of these 3NF's to reproduce the ^{3}H binding energy, it was possible to get essentially correct the bindings of ^{3}He and ^{4}He. Also a fairly successful description of low energy bound state energies of up to $A=8$ nuclei resulted when adding 3NF's. This was recently improved by adding further 3NF's related to three-pion exchange with intermediate Δ's [33].

Though this first signal on 3NF effects resulting from discrete states is important, a more sensitive and detailed investigation of 3NF properties must be carried out in 3*N* continuum. From the theoretical side, one can make exact predictions for various observables of the elastic nucleon-deuteron (Nd) scattering and of the Nd breakup process, using nuclear forces in all their complexities [3]. Experimentally, one can nowadays access spin observables in elastic Nd scattering, where in the initial state the deuteron and/or the nucleon is polarized and where in the final state also the polarizations of the outgoing particles can be measured [34–42]. These, together with the elastic scattering cross sections, lead to a very rich set of observables in Nd elastic scattering, which provides a solid basis to test the models of the 3*N* Hamiltonian. Such a test study has been performed [43], showing that the current 3NF models exhibit large effects and that more data are needed to provide constraints on the theoretical models of 3NF's.

First data sets [44,34,37–39] in elastic Nd scattering showed both successes and failures of present day 3NF models combined with the realistic *NN* forces. This study was extended in Refs. [45–47] to the cross section and several spin observables of the kinematically complete Nd breakup process, and sensitivity of breakup observables to 3NF's combined with the high-precision *NN* interactions have been studied. In the theoretical study [49,50,48] of the entire phase space of the breakup process at several energies, the regions in phase space where the largest 3NF effects occur have been located. These regions are in general different for the various observables. It was found that the 3NF effects increase in general with energy. Among the observables, the five-fold differential cross section turned out to be a promising one to observe 3NF effects. In Refs. [50,48] the existing data have been compared to theoretical model predictions. It was found that, based on experiments performed so far, it is rather difficult to find by chance a configuration with large 3NF effects. As the dataset for the Nd breakup is of much poorer quality than the elastic scattering one, new high-precision data, covering a large part of the breakup phase space, are required. To enrich significantly the existing breakup dataset, the ^{1}H$(\vec{d}, pp)n$ breakup experiment has been performed at KVI in Groningen, using a beam of 130 MeV polarized deuterons. This experiment covers a large fraction of the full breakup phase space. High-precision cross sections together with vector and tensor analyzing powers have been measured in kinematically complete configurations, detecting two outgoing protons in coincidence. In this paper we present the unpolarized cross-section data for 38 kinematically complete configurations and compare them to modern force predictions. Presentation of the results for the analyzing powers is postponed until precise enough calibration of the beam polarization can be made.

The paper is organized as follows. In Sec. II the details of the experiment and of the data analysis are described. We briefly present in Sec. III the theoretical formalism underlying 3*N* continuum Faddeev calculations. Our high-precision breakup cross-section data are presented and compared to theoretical predictions in Sec. IV. We conclude and summarize in Sec. V.

II. MEASUREMENT AND DATA ANALYSIS

A. Experimental setup

The experiment was performed at the Kernfysisch Versneller Instituut (KVI), Groningen, The Netherlands. The beam of vector and tensor polarized deuterons was produced in the atomic-beam–type polarized ion source POLIS and accelerated in the superconducting cyclotron AGOR. Since in the present analysis only cross-section values are reported, the beam polarization is irrelevant here and will not be discussed further. It suffices to mention that eight different polarization states of the deuteron beam (combinations of vector and tensor polarizations) have been used and the actual polarization status has been recorded for every event. The intensity of the deuteron beam, with an energy of 130 MeV, was kept around 50 pA, to maintain a favorably low level of accidental coincidences.

The deuteron beam was focused to a spot of approximately 2 mm diameter on a liquid hydrogen target, operated at the temperature of 15 K and about 140 mbar pressure [51]. The target cell was made of high purity aluminum for optimizing the thermal conductivity. To minimize the background contribution originating from the target windows and the energy losses of the reaction products, a synthetic Aramid foil of 4 μm thickness was used as target windows material. The thickness of the target cell filled with liquid hydrogen was 4.5 mm. During the measurement, the target was continuously wobbled in the plane perpendicular to the beam axis in order to decrease the local heating caused by the energy loss of beam traversing the target. The cell had an elliptical shape (with the axes of 20 mm and 30 mm) to accommodate the amplitude of the wobbling motion. To exploit this feature, the whole target assembly (cold head, gas leads) was interfaced to the scattering chamber, evacuated to 10^{-6} mbar, via a flexible bellow, located approximately in the middle of the scattering chamber. To allow the charged reaction products to leave the vacuum, the chamber was closed with a Kevlar/Aramica foil window of 130 μm effective thickness. The window is equipped with a central opening with a flange connection to a specially shaped beam pipe that passes through the whole detection system and provides an

evacuated path for the transport of the primary beam to the Faraday cup that is located several meters further downstream.

The SALAD (small angle large acceptance detector) detection system [52] is optimized for registering and identifying the charged reaction products. In its application for the breakup measurement, it consists of a three-plane multiwire proportional chamber (MWPC) [53] and two layers of scintillator hodoscope. The whole detection system is shown schematically in Fig. 1. The MWPC is used for precise reconstruction of the charged particle emission angles. To resolve reconstruction ambiguities for multihit events, it consists of three anode wire planes with wires spanned horizontally (x), vertically (y), and diagonally (u). The anodes are built of gold-plated tungsten-rhenium wires of 20 μm diameter that are spaced 2 mm apart. Each wire plane is sandwiched between two cathode frames that are made of sprayed-graphite coated mylar foils with the thickness of 25 μm. The anode-cathode spacing is 4 mm and the distance between the subsequent anode planes is 12 mm. The first anode was placed at the distance of 300 mm from the target. The active area of the MWPC is 380×380 mm^2 with exclusion of the central hole of 97.2 mm in diameter. A gas mixture of 80% CF_4 and 20% isobutane was used. The chamber was operated at a pressure of 2–3 mbars above atmospheric pressure. The almost pointlike reaction region, as compared to the target-MWPC distance, allowed for reconstruction of the polar and azimuthal particle emission angles with the overall accuracy of 0.6°. The plastic scintillator hodoscope consists of 24 transmission detectors (ΔE strips) and 24 stopping detectors (E slabs). All ΔE strips (plastic scintillator BC-408) are 2 mm thick and 60 mm wide; 20 of them are 400 mm long while four central ones are shorter, of 345 mm length, to accommodate the central beam pipe. Light from each of these 24 scintillators is read out from one side by an XP2020 photomultiplier, coupled optically to the thin scintillator via a prismatic light guide of optimized shape. The E detectors are plastic scintillator (BC-400) slabs, covering a section of a cylindrical wall with the inner radius of 915.5 mm. The system consists of 24 thick plastic prisms with a thickness of 112.5 mm, length of the sides 61.2 mm and 68.7 mm, and a height of 436 mm each. Four central slabs are shorter to leave space for the beam pipe. Light is collected from each slab by an XP2282 photomultiplier via 160 mm long light guide. The thickness of the E counters is sufficient to stop protons with energies up to 130 MeV in the whole angular range covered by the detection system. The energy resolution of the E counters is about 5%. The ΔE strips are arranged perpendicularly to the E slabs (cf. Fig. 1), forming together a two-dimensional array of 140 elements, with an area of about 60×60 mm^2 each. The hodoscope covers the range of polar angles between 10° and 35° and the full range of azimuthal angles. Information from this telescope array was used for particle identification, determination of their energy, and for trigger definition (see below).

The electronics system was designed to identify and selectively reduce rates for different kinds of events, originating in both elastic scattering and breakup reaction. The most relevant part of the trigger electronics is shown in Fig. 2.

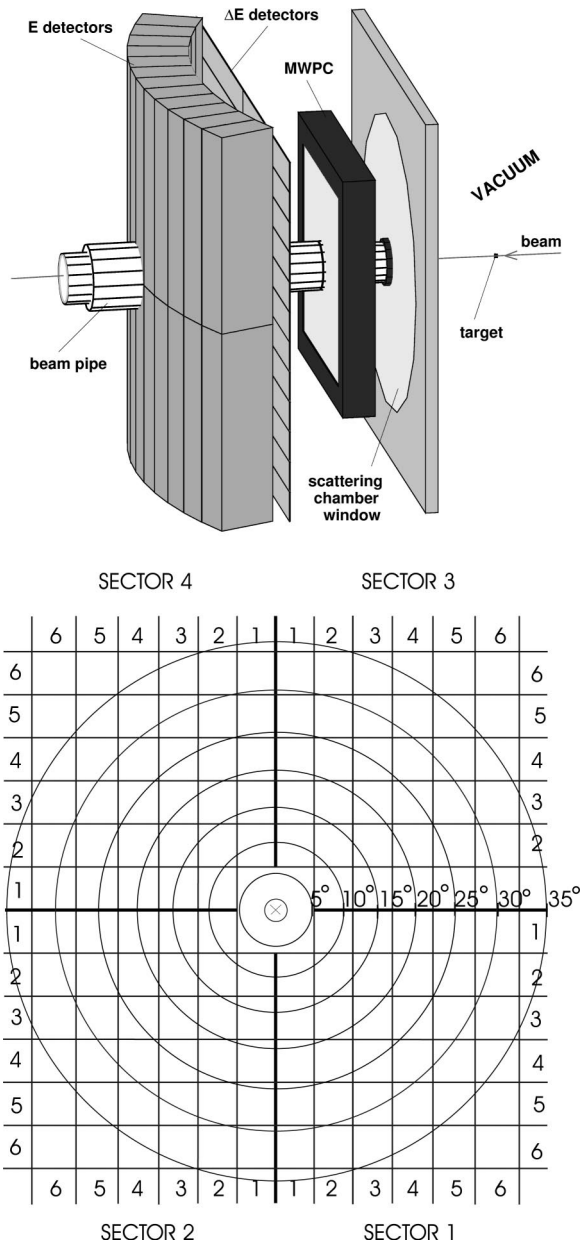

FIG. 1. Schematic view of the detection system (upper part), presenting the positions of the MWPC, the scintillation detectors, and the scattering chamber window, with the central beam line indicated. A projection (along the radii from the target center) of E detectors on the plane of ΔE counters, is shown in the lower part of the figure. The resulting two-dimensional array of 140 detection elements is presented, together with circles representing polar angles covered by the system with respect to the target position.

Trigger conditions were constructed on the basis of the hodoscope information alone, while the MWPC data were used off-line for detailed event classification. The signal from every photomultiplier was split in two: one was directed to the corresponding analog-to-digital converter (ADC) input for integration (energy information), while the other was connected to the constant fraction discriminator (CFD) input. Outputs of the discriminators were used for three purposes: individual detector count rates recording in CAMAC scalers, time-of-flight measurement (with respect to the cyclotron rf

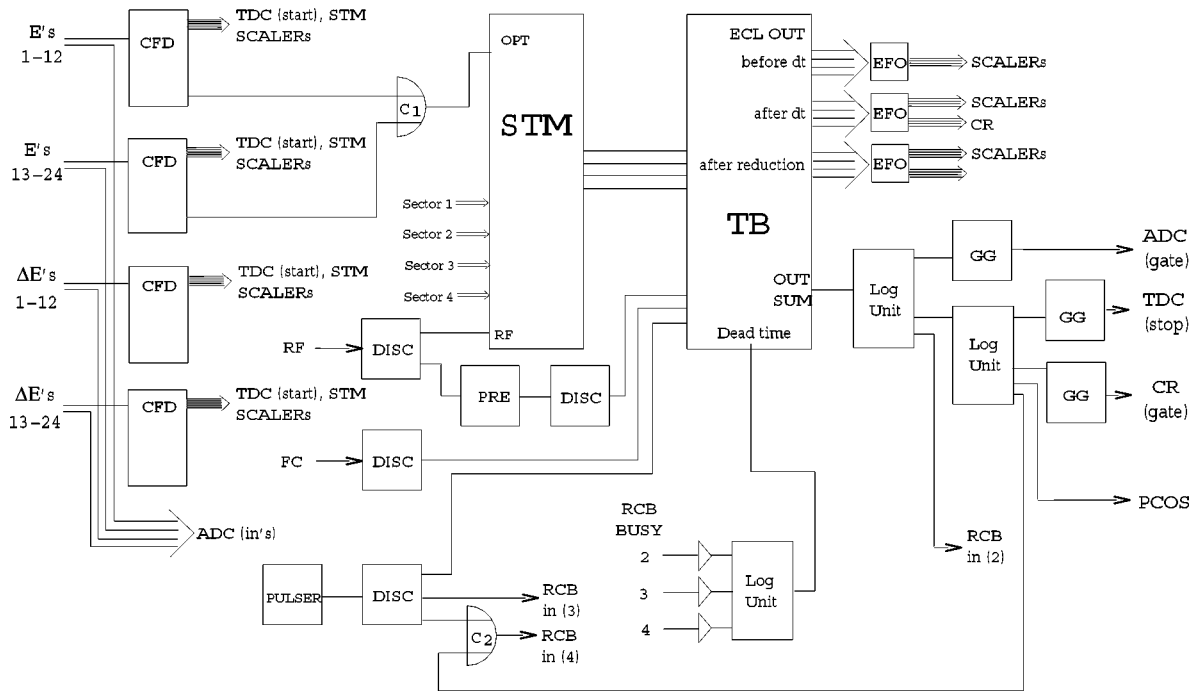

FIG. 2. Simplified diagram of the main trigger electronics system.

signal), and for actual trigger definition in the so-called SALAD trigger module (STM) [54]. This module, containing five memory lookup units (MLU—16-bit address-space memories), was originally designed to provide a multiplicity trigger in bremsstrahlung experiments, but with appropriate input order matching and programming it suited the breakup experiment perfectly. Each discriminator signal acted as a bit, signaling status of the particular detector in every event. Our purpose was to distinguish roughly between the events, in which only one charged particle reached the detector (single events) and coincident events, when the hodoscope registered two charged particles in the defined time window. In this last class we could distinguish between candidates for elastic scattering (events characterized by relative azimuthal angle of 180°) and breakup events (two "hits" at any angle combination). By appropriately programming the MLU's content we were able to identify events with proper pattern of $\Delta E-E$ coincidences and with required multiplicity. This identification was reflected in a 3-bit output of the STM, in which three mutually exclusive bits carried information on registering a single, elastic or breakup event, respectively. Details of the events classification can be found elsewhere [55].

Determination of the input pattern was performed within a 55 ns wide time window, opened by a fast OR signal from all CFD's of the stopping detector. Such coincidence time window was chosen in order to accommodate particles produced in two consecutive beam bursts (rf of the cyclotron is 38.5 MHz), thus providing a possibility to determine the accidental coincidences rate. Typically, the strobe rate was about 7×10^5 s^{-1}, out of which about 85% was due to single events while breakup and elastic coincidences contributed both on the level of 7%. Proportions of the event classes were changed to enhance contribution of coincidences and to reduce the total trigger rate to a level acceptable by the data acquisition system with the use of downscaling module (module TB in Fig. 2), which also took care of rejecting valid triggers during the readout initiated by the previously accepted one. After downscaling, the resulting logic sum of all triggers was used to define common signals for the readout system (gates for ADC's, common stop for TDC's, gate for the coincidence register storing the trigger patterns for each event, and gate for the MWPC readout system) and to interrupt the front-end processor to execute the readout procedure.

The MWPC was equipped with the PCOSIII readout system, consisting of the amplifier/discriminator cards mounted directly on the chamber, coupled with the latch modules, storing the hits occurring on the wires. The latch modules are hosted in a dedicated CAMAC crate, interfaced to the data acquisition by a dedicated controller and CAMAC interface module. The hits are coded in a way to enable an unambiguous identification of every hit wire.

In response to every accepted trigger the digitized pulse height (energy) and time information from ADC's and TDC's were transmitted to a dual-port VME memory module and readout by the front-end processor. Information from the PCOS system (centers and widths of the groups of hit wires), together with the coincidence register data, were read out via CAMAC bus and the VME CAMAC branch coupler. Both pieces of information, supplemented with additional words (synchronization, polarization state, etc.) were combined into a single event record and stored on the magnetic tape. Periodically (every 1 s), another kind of trigger signal was generated to induce the readout of scalers, recording detector rates and additional information like trigger rates, integrated beam current, and pulse generator signals for dead-time monitoring. Target pressure and temperature as well as posi-

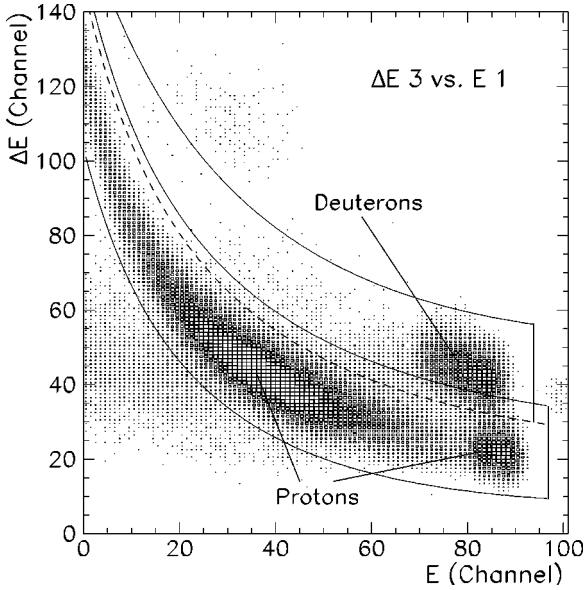

FIG. 3. An example of $\Delta E-E$ particle identification spectrum for one of the 140 telescopes, covering the angular range $\theta=13.9°-21.6°$, $\phi=66.3°-90°$. Definitions of areas, within which a particle is identified as a proton or as a deuteron, are shown as "banana-shaped" gates. Breakup protons were accepted within the lower solid-border contour. For the case of selecting the elastic scattering events the border between the proton and deuteron gates was shifted to the middle of the valley between their regions, indicated by the dashed line.

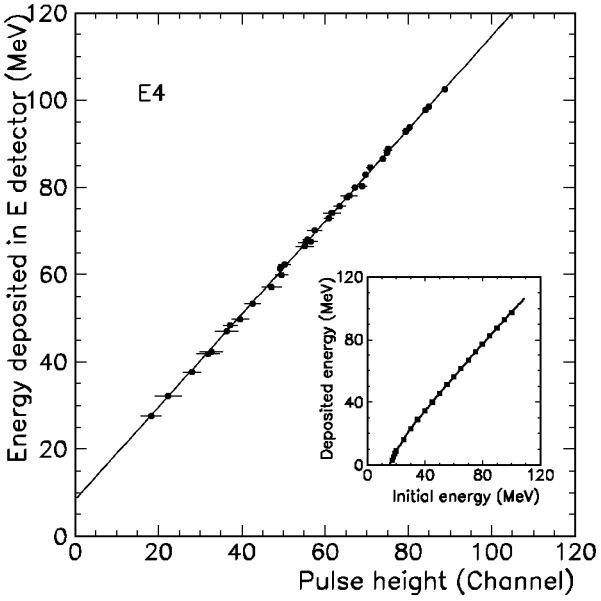

FIG. 4. Dependence of the deposited energy on pulse height for one of the 24 E detectors. The line represents the linear fit to the measured calibration points. Inset: the energy deposited by protons in the stopping detector as a function of their energy at the moment of the reaction. For clarity, the results for only one proton emission angle $\theta=20°$ are shown.

tion of the beam on the target were controlled continuously throughout the whole experiment by means of autonomous control systems.

B. Data analysis

1. Event selection and energy calibration

The events of interest for the analysis of this experiment are the coincidences of two charged particles, i.e., proton-proton pairs from the breakup process or, necessary for cross section normalization, deuteron-proton pairs from the elastic scattering. In further analysis only the events registered in a well-defined, 20-ns-wide time window set on all time spectra were accepted. In this way only the products of the reactions initiated within a single beam burst were selected.

Particle identification was based on the $\Delta E-E$ technique. For that purpose ΔE versus E spectra were built for each telescope, i.e., for coincidences of every ΔE strip with every overlapping E slab (see example in Fig. 3). For all 140 telescopes very good separation between protons and deuterons was observed in the whole energy range. For analysis of elastic scattering the curve separating protons from deuterons was placed in the middle of the valley between their branches (dashed line in Fig. 3). When selecting the breakup events the area defining protons was chosen to be wide enough to avoid any loss of protons (solid line in Fig. 3). Since the elastic scattering kinematics defines uniquely the angular correlation between proton and deuteron and the discussed angular configurations of the breakup reaction are very different from the elastic scattering ones, such broadening of the proton gate did not lead to misidentification of the breakup coincidences. The events lying outside the condition areas of protons or deuterons were rejected.

In order to obtain the breakup cross section as a function of proton energy or, equivalently, as a function of the arclength S along the kinematical curve, energy calibration in the whole investigated range is required. Since energies of the elastically scattered protons registered in our system were generally higher than the ones from the breakup reaction, special calibration runs with energy degraders were performed. The degraders were made of steel plates with precisely known (better than 1%) thicknesses between 1 mm and 15 mm. The positions of the peaks corresponding to protons from the elastic scattering which traversed the degraders were compared with the results of simulations taking into account all energy losses of protons on their paths from the reaction point to the detectors. For each of the 24 E detectors an individual calibration line was fitted to about 45 calibration points (see example in Fig. 4). No significant departures from linearity were observed. However, for measurements made with thick degraders, the straggling effects become relevant, and determination of the peak position is biased with larger uncertainties. This is depicted in Fig. 4 by larger horizontal error bars of the calibration points obtained in such conditions.

In the next step the relation between the energy deposited by protons in the E counter and their energy at the moment of the reaction was found by Monte Carlo simulation of the energy losses. For this purpose protons with fixed energy were generated at a given θ emission angle, in the range from 10° to 40°, in steps of 5°. A dependence of the deposited

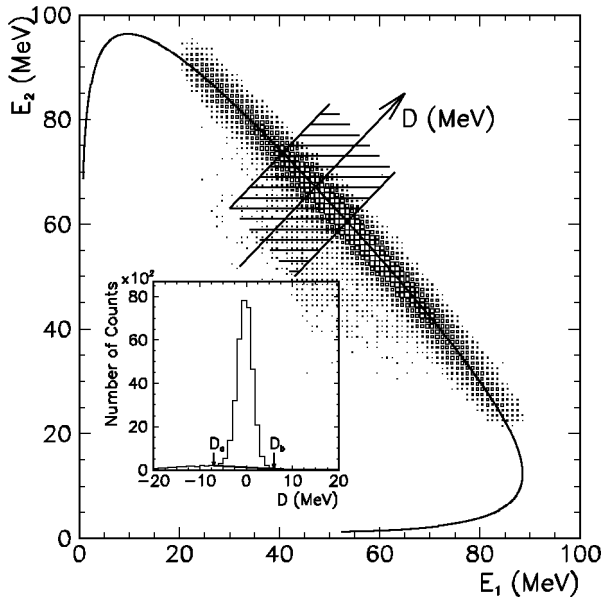

FIG. 5. E_1 versus E_2 coincidence spectrum of the two protons registered at $\theta_1=20°\pm1°$, $\theta_2=15°+1°$, and $\phi_{12}=90°+5°$. The solid line shows a three-body kinematical curve, calculated for the central values of the experimental angular ranges. Inset: determination of the accidental coincidences. The spectrum was obtained by choosing one slice along the kinematical curve in the spectrum E_1 vs E_2 (marked area in the main figure) and projecting the events onto the D axis. A linear function between the two limits of integration, D_a and D_b, represents the assumed level of accidental coincidences to be subtracted.

energy on the energy at the moment of reaction for $\theta=20°$ is shown as an example in the inset in Fig. 4. By combining both steps we can convert the registered pulse height to the energy of protons emitted from the reaction. Applying this calibration to three-body kinematical curves of the breakup reaction showed that a small, linear correction of calibration is required. This correction, common for all the detectors, amounts to only 1.2 MeV for the deposited energy of 50 MeV and allows for a consistent description of the energy spectra for both two-body and three-body processes. In view of the previously discussed larger uncertainties of the calibration points at low values of the deposited energy, such a correction, lying well inside the estimated error of the calibration function, is fully justified. Figure 5 shows an example of the E_1-E_2 coincidence spectrum with the calculated kinematical curve perfectly following the data subjected to the corrected calibration.

After selection of the proton-proton coincidences and having performed the energy calibration, practically any kinematical configuration of the breakup reaction within the angular acceptance of the detection system can be analyzed. The configuration is defined by emission angles of the two outgoing protons: two polar angles θ_1 and θ_2 and a relative azimuthal angle ϕ_{12}. The azimuthal ϕ and polar θ angles for every registered particle were calculated from the MWPC information, i.e., from coordinates of hit wires in x, y, and u planes. To avoid ambiguities in correlating the active x and y wires when more than one particle was registered, the status (active or not) of an appropriate u wire was checked. In comparing of the expected and registered u values a tolerance of up to ±3 wires was allowed to take into account possible small angle scattering effects.

The kinematical spectra E_1 vs E_2 as shown in Fig. 5 were built for each analyzed configuration. The angular range for integration of events was chosen to be $\Delta\theta_1=\Delta\theta_2=2°$ and $\Delta\phi_{12}=10°$, which was wide enough to reach required statistics, while variations of the cross section within this range are still small. In this way the experimental cross sections can be compared with the theoretical predictions calculated for the central values of the analyzed angular range. The energies E_1 and E_2 of each event can be transformed into two new variables: D denoting the distance of the (E_1, E_2) point from the kinematical curve in the E_1-E_2 plane, and S the value of the arclength along the kinematics with the starting point ($S=0$) chosen arbitrarily at the point where E_2 reaches its minimum. Events in slices along the S axis were projected on the central D axis, as shown in Fig. 5. In the resulting spectra (inset in Fig. 5), the breakup events group themselves in a prominent peak underlaid with a low background of accidental coincidences, which was checked with the help of accumulated accidental coincidence events from two neighboring beam bursts. This background changes smoothly and was approximated by a linear function. The choice of integration limits D_a and D_b as well as of the assumed background function, is not critical since the contribution of accidental coincidences in all analyzed angular configurations was very low, varying between 2% and 5%.

2. Efficiencies

Detection of a charged particle in the MWPC has a finite efficiency, which varies across the wire chamber active area. It can also happen that during the experiment some wires become inefficient and decrease the overall efficiency. In order to correct for such effects a map of the MWPC efficiency was constructed with the use of registered single events. The efficiency of each individual plane can be found by determining θ and ϕ angles from hits in two other planes and checking whether the corresponding hit in the investigated plane is present. Such a procedure was performed by counting the number of events in the angular segments of $\Delta\theta=1°$ and $\Delta\phi=5°$. The probability of registering a particle in a given MWPC plane, for example, in the x plane, for a given angular segment is

$$\epsilon_x(\theta, \phi) = \frac{N_{xyu}(\theta, \phi)}{N_{yu}(\theta, \phi)}, \tag{1}$$

where $\epsilon_x(\theta, \phi)$ is the efficiency for particle detection in the x plane in a segment centered at coordinates (θ, ϕ). $N_{xyu}(\theta, \phi)$ is the number of events registered in this segment with at least one wire hit in each plane x, y, and u, taking into account the necessary correlation of the wires, as discussed above. $N_{yu}(\theta, \phi)$ is the number of events registered in this segment with at least one wire hit in plane y and one in plane u.

The efficiencies of y and u planes were calculated in a similar way, differing only in the denominator. The total

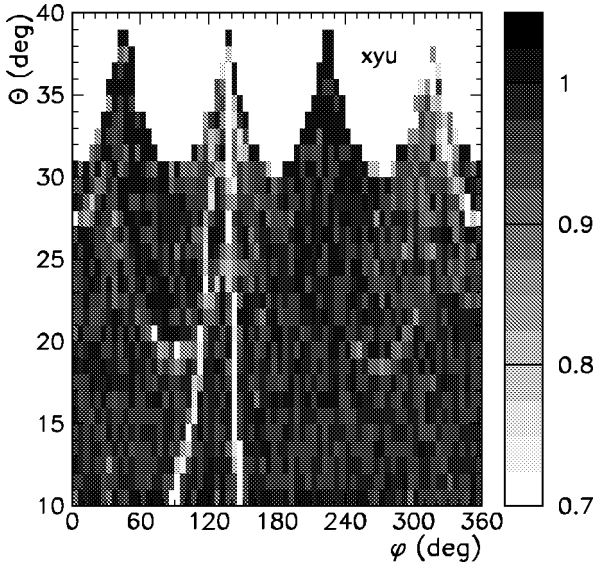

FIG. 6. Efficiency map for the MWPC as a function of the angular coordinates.

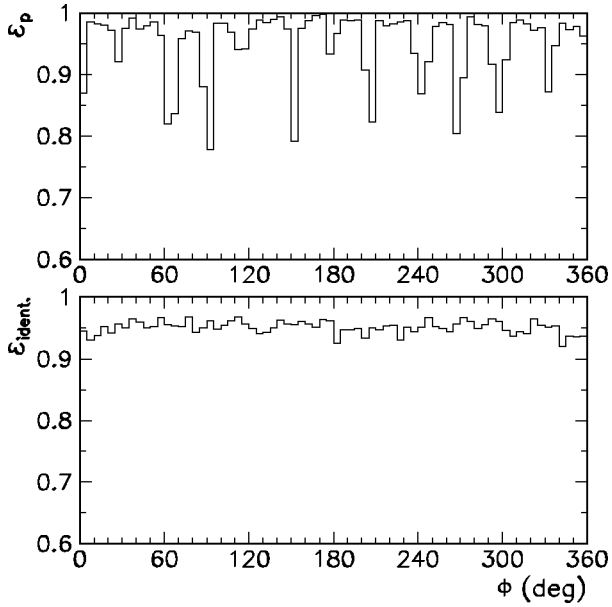

FIG. 7. Efficiencies of the scintillation detector hodoscope for a region of $\theta=15°\pm0.5°$, as a function of the azimuthal angle. Upper part: detection efficiency; lower part: particle identification efficiency. Statistical uncertainties are negligible.

MWPC efficiency was obtained as a product of the probabilities for particle registration in the individual planes:

$$\epsilon_{xyu}(\theta,\phi)=\epsilon_x(\theta,\phi)\epsilon_y(\theta,\phi)\epsilon_u(\theta,\phi). \quad (2)$$

Figure 6 shows the efficiency map for the whole MWPC detector. The MWPC efficiency is generally above 95%, but for regions of a few inactive wires it falls down dramatically to about 70%. Due to the square shape of the MWPC the angular range of θ between 30° and 44° is only partially covered in azimuthal angle ϕ (see empty regions in Fig. 6). The MWPC efficiency was determined with statistical accuracy of 0.3%.

Similar to MWPC, the detection efficiency in each part of the $\Delta E-E$ array should be determined. The main factor which affects the efficiency is the hodoscope granularity, in particular, gaps between ΔE detectors. If a particle crosses the detector plane exactly through a gap it is not detected in the ΔE detector and thus particle identification cannot be performed. The hodoscope detection efficiency map was determined by studying coincidences of two protons reaching neighboring sectors (cf. Fig. 1), which assured that proton-deuteron coincidences were absent. First, an arbitrarily chosen "region of reference" was defined on the basis of the angular information from the MWPC. Presence of full information for the particle registered within that reference region was required, that is, its energy and timing information from ΔE and E detectors as well as a complete set of hits from the MWPC. In the investigated region, defined again with the use of the MWPC, one compared the numbers of two kinds of coincidences with the proton detected in the reference region: full, with complete ΔE and E information and incomplete, with the ΔE information missing for the particle detected in the investigated region. This procedure allowed us to determine the hodoscope detection efficiency with the statistical accuracy of 0.3%. A projection of 1° wide bin of the hodoscope detection efficiency map for $\theta=15°$ is shown in Fig. 7, upper part. The efficiency is close to 1 for large areas of the detector, however, it drops rapidly to even 0.8 for the regions influenced by ΔE detector gaps.

As mentioned in Sec. II B 1 and shown in Fig. 3, there exist a certain probability of misidentifying the registered particle when applying the $\Delta E-E$ technique. Efficiency for particle identification was determined similarly as the hodoscope detection efficiency, which was based on the fact that in the neighboring sectors no real proton-deuteron coincidences can be observed. Therefore, by comparing the numbers of identified protons and deuterons, the proton identification efficiency was determined. The efficiency is very stable, around 0.95 for the whole detector, see an example in the lower part of Fig. 7.

3. Cross-checks of the geometry of the setup

Knowledge of the precise values of θ and ϕ emission angles of the outgoing particles is very important for reconstructing the breakup event kinematics. The question arises of how significantly geometrical inaccuracies of the system can affect the analysis of the breakup events. The distance Z between the MWPC and the target could introduce some uncertainty, especially since the target cell in the scattering chamber was suspended on a flexible holder and its perfect positioning in the geometrical center of the scattering chamber was not guaranteed. Since there exists unique dependence between the angles of the scattered proton and deuteron, we analyzed elastic scattering events with various assumed Z distances. We compared the plots of the reconstructed θ_p versus θ_d with calculated kinematical curves of the dp elastic scattering, performing χ^2 consistency test (see example plots in Fig. 8). Inspecting the dependence of the χ^2 values on the distance Z, we found that the actual distance between the target center and the MWPC (300 mm) can be

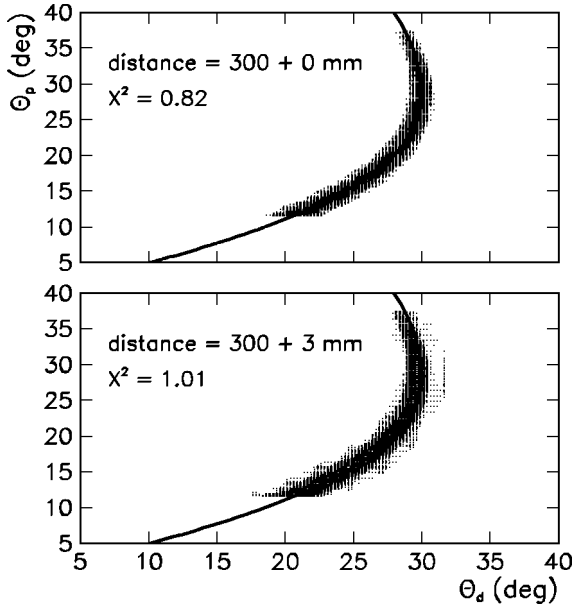

FIG. 8. Comparison of the kinematical curve of the elastic *dp* scattering with the data analyzed under assumption of two different distances between the MWPC and the target center. The agreement between the data and the curve is quantified in terms of the mean square distance per degree of freedom and shown in the figure.

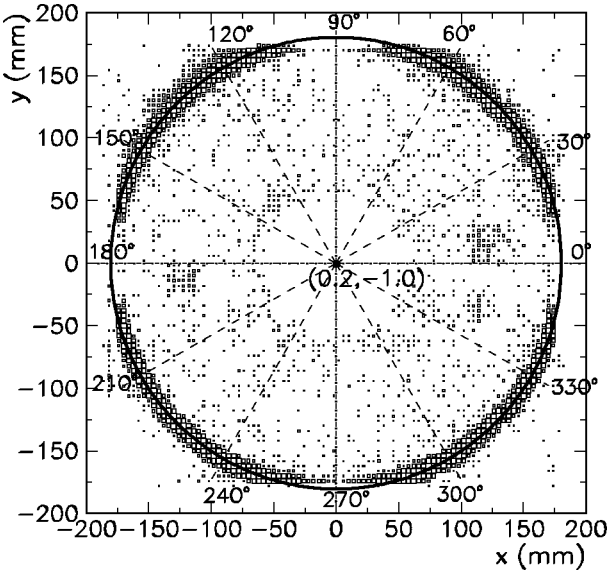

FIG. 9. Image of deuteron hit positions at the MWPC obtained under the condition that the coincident proton is registered at relative ϕ_{pd} angle of $180° \pm 5°$ and at $\theta_p = 29° \pm 3°$. The center of the circle and its radius have been fitted to the data. The indicated center position reflects the shift (in mm) of the beam axis with respect to the MWPC center.

verified with the precision of about 1 mm. This finding confirms also a reliability of the reconstructed θ angle (with accuracy much better than 0.3°) and is an example of self-testing ability of our system.

Using the angular information for the elastically scattered particles, a check of the relation between the beam axis and the geometrical axis of the MWPC was performed. Due to kinematical relations for the elastic scattering process with beam particle heavier than the target, the maximum concentration of deuterons is near the emission angle $\theta_d = 30°$. By selecting θ_p angles of the elastically scattered protons between 26° and 32° we obtain a very narrow angular range of deuteron emission from 29.83° to 30.03°. Since our detection system is highly symmetric, these deuterons should group in a well-located ring with the center at the geometrical center of the MWPC. We have limited our analysis to the area where this ring is not distorted by decreasing efficiency near the edges of the MWPC (diagonal dashed sectors in Fig. 9). The circle, which is fitted to the experimental distribution, is centered at $(0.2, -1.0)$ mm and stays stable for all data files. Estimated accuracy of the extracted coordinates of the center is below 0.5 mm. By combining the circle radius with the known scattering angle, one obtains the distance between the target and the MWPC. The result is consistent with the check described earlier. The 1 mm shift of the MWPC in the vertical direction has been corrected for in the data analysis.

4. Cross section normalization

The breakup cross-section normalization is made with the use of the known *pd* elastic scattering cross section data [56]. Therefore, a crucial quantity to be determined experimentally is the number of the elastic scattering events. In order to correctly select elastic scattering coincidences both proton and deuteron had to be properly identified. However, fully identified deuteron-proton coincidences were registered only in a limited range of proton θ_p angles, since low-energy deuterons were stopped in ΔE detectors and thus could not have been recognized in particle identification procedure. In order to broaden the range of identified elastic scattering events, we have included in the analysis also the events where one particle was recognized as a proton while the second one was stopped in ΔE, fulfilling the kinematical conditions of the elastic scattering.

For events classified as originating from the elastic scattering, their energy distribution spectra were built in angular bins of $\Delta\theta_p = 1°$, see example in Fig. 10. A linear background function was assumed (see inset in Fig. 10) and subtracted from the number of counts obtained by integration in the interval defined by the limits selecting the peak. Typically, the background contribution was around 1.5% for all polar angles relevant for normalization.

In order to check quality of the procedure of selecting the elastic scattering data, the shape of the obtained elastic scattering angular distribution was compared with the data of Shimizu *et al.* [56]. Figure 11 shows our angular distribution as a function of θ_p, multiplied by an arbitrary factor (no absolute normalization of the elastic scattering cross section was performed in this experiment). It can be seen that the overall agreement is satisfactory except for, maybe, forward angles $(13° - 20°)$. In that range no deuteron identification was possible, thus an admixture of breakup events cannot be excluded, which could lead to slightly too large values of the cross section. Therefore, for normalization of the breakup cross section, we decided to use only the elastic scattering cross section for $\theta_p > 20°$.

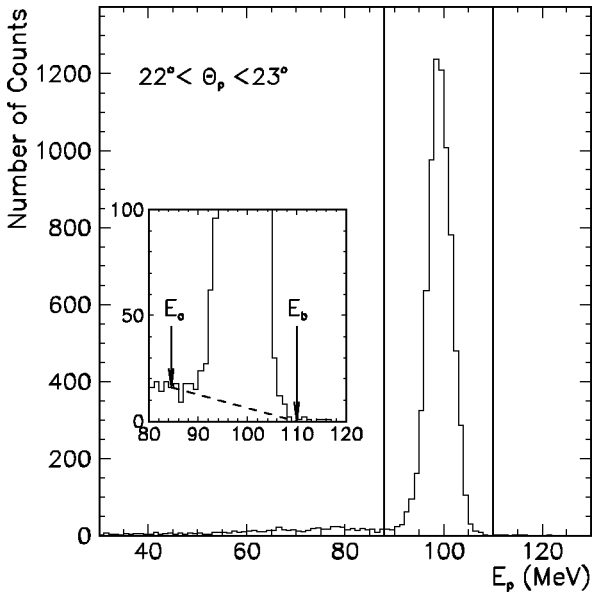

FIG. 10. Energy spectrum of the elastically scattered protons obtained in a 1° wide bin of the proton θ_p angle, as indicated in the figure. The spectrum was obtained under the following conditions: $\phi_{pd}=180°\pm5°$, one particle identified as a proton and the second one identified as a deuteron. Vertical lines represent the integration limits for the cross-section evaluation. The inset demonstrates the background subtraction method, with a linear function defined by the integration limits (arrows E_a and E_b correspond to the vertical lines in the main figure).

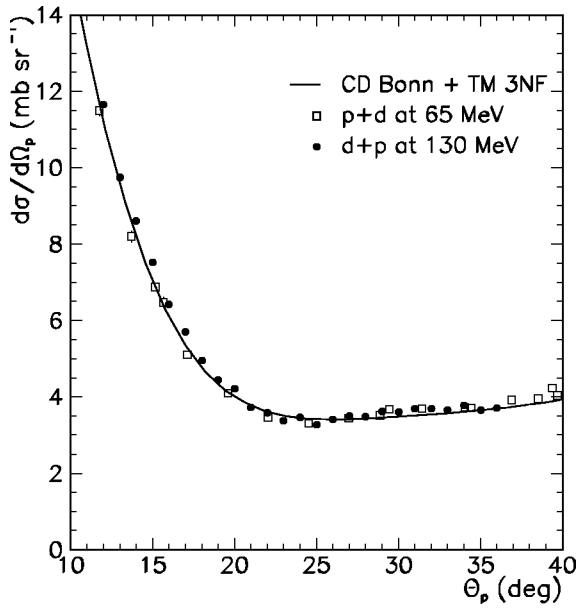

FIG. 11. Angular distribution of the elastic scattering events. Our experimental distribution is multiplied by an arbitrary factor and shown in terms of the cross section values (full circles). Statistical errors are smaller than the point size. Empty squares represent the cross-section measured by Shimizu *et al.* [56]. Solid line shows the results of calculations with the CD Bonn potential and the TM 3*N* force model.

Simultaneously measured coincidences from the breakup and elastic scattering reactions allow us to express the breakup cross section in terms of the elastic scattering one and both measured coincidence rates. In such an approach we profit from cancellation of common factors which are difficult to determine exactly separately and which would be a source of systematic uncertainties. Thus, in the final formula below, the integrated beam current, the density, and thickness of the target as well as the dead-time correction are absent and the differential breakup cross section for a chosen angular configuration is given by

$$\frac{d^5\sigma}{d\Omega_1 d\Omega_2 dS}(S,\Omega_1,\Omega_2)=\frac{d\sigma_{el}}{d\Omega_1}(\Omega_1)\frac{N_{br}(S,\Omega_1,\Omega_2)}{N_{el}(\Omega_1)}\times\frac{\Delta\Omega_1^{el}}{\Delta\Omega_1\Delta\Omega_2\Delta S}\frac{\epsilon^{el}(\Omega_1^{el})\epsilon^{el}(\Omega_2^{el})}{\epsilon(\Omega_1)\epsilon(\Omega_2)}, \tag{3}$$

where N_{br} is the final number of breakup coincidences registered at the angles Ω_1,Ω_2 and projected onto a ΔS-wide arclength bin. Subscripts 1 and 2 refer to the first and the second protons registered in coincidence or to the proton and the deuteron in the case of elastic scattering. $\Omega_i=(\theta_i,\phi_i)$ are the polar and azimuthal angles, respectively, and $\Delta\Omega_i$ is the solid angle ($\Delta\Omega_i=\Delta\theta_i\Delta\phi_i\sin\theta_i$). Products $\epsilon(\Omega_1)\epsilon(\Omega_2)$ [or $\epsilon^{el}(\Omega_1^{el})\epsilon^{el}(\Omega_2^{el})$] contain all relevant efficiencies, as discussed previously. N_{el} is the final number of elastic scattering coincidences registered at the proton angle Ω_1^{el}. The elastic scattering cross section $(d\sigma_{el}/d\Omega_1)(\Omega_1)$ is taken from Ref. [56]. The bin width ΔS was chosen to be 4 MeV. It should be noted that N_{br} and N_{el} are obtained from the experimentally determined numbers of coincidences for breakup and elastic scattering, respectively, by individual background subtraction and then by multiplying by the corresponding downscaling factors applied in the experiment (cf. Sec. II A).

5. Experimental uncertainties

Statistical errors for the measured cross-section distributions comprise the error of the measured number of the breakup coincidences, as well as statistical uncertainties of all quantities used in the normalization, i.e., the number of the elastic scattering events and all efficiencies included in Eq. (3). This total statistical error is of the order of 1.5% for the value of the cross section of about 0.5 mb MeV^{-1} sr^{-2} and smaller for larger cross sections.

The influence of systematic errors was reduced significantly by detailed analysis of the geometry of the setup and of the total detection efficiency. The remaining main possible sources of uncertainties are discussed below.

With the help of the elastic scattering data we have checked the influence of the beam polarization on the cross section values. By comparing the results of analysis for the nominally unpolarized beam and averaged over all polarization states we have concluded that the averaging is very efficient, introducing an uncertainty of at most 1%. Including the data accumulated with the polarized beam reduces the statistical uncertainty by a factor of 3.

The shape (length) of the breakup cross-section distribution (as a function of S) can be affected by uncertainty of the energy calibration. This effect was estimated by comparing values of the breakup cross section calculated with the corrected calibration parameters to the ones obtained with the original calibration parameters. These effects are small and do not exceed 0.01 mb, i.e., 2% for typical values of the measured cross sections.

Subtraction of accidental coincidences, performed for separate slices along S curve, may affect both the shape and the overall height of the cross-section distribution, although the low level of background leaves not much room for inducing significant uncertainties. Sensitivity of the result to the choice of integration limits of the breakup peak (being simultaneously the fixing points for the background determination and subtraction, see Fig. 5) was checked by varying them by ±1 MeV. In all cases the number of the breakup events varied well within the limits of the statistical accuracy, by less than 0.5%. The resulting systematical error of the contribution of the accidental coincidences and thus of their subtraction procedure can be neglected.

Uncertainty of the reconstructed angle originates from angular resolution, finite target thickness, size of the beam spot on the target, and straggling effects. The angular resolution is given by the distances between wires in the MWPC and, for polar angles, reaches maximally 0.3°. The effects of finite volume in which the reactions take place and of the angular straggling were simulated using the GEANT package, with the conclusion that they do not exceed 0.5°. The mentioned effects cause a spread of the angular distribution but do not lead to a systematic shift. Correct reconstruction of θ angles is supported by the well-reproduced angular dependence of the cross section for the elastic scattering and the shape of the two-body kinematics. Discreteness of the position information delivered by the MWPC influences also the effective solid angle determination. It was calculated that the corresponding systematic error is 1.3−2.0 %.

Sets of proton emission angles for the breakup configurations presented in this work are very different from the ones for proton-deuteron coincidences of the elastic scattering. Therefore the particle identification area could have been set wide enough to avoid any proton loss (cf. Sec. II B 1). Other losses, such as inefficiencies of the detection system, were calculated and corrected for. Their contribution to the overall systematic uncertainty is below 0.5% and can be neglected.

Uncertainty in determination of the elastic scattering rates influences directly the cross section normalization. Accidental coincidences contribute to the peak of elastically scattered protons at still lower level than in the breakup case, and the error introduced while subtracting them can be neglected. As an additional check of accuracy of the elastic scattering rates, a comparison of the shape of our elastic scattering cross section to the one obtained by Shimizu *et al.* was made. For the angles $\theta_p > 20°$, where full identification of proton-deuteron coincidences is possible, the maximal deviation reaches 2.5%. The errors of the reference elastic scattering cross section of Shimizu *et al.* are another source of the systematic uncertainty of 1.6%. Finally, estimated total systematical normalization uncertainty is 1.6–3.0 %.

TABLE I. Summary of the relevant experimental cross-section uncertainties.

Source of uncertainty	Magnitude (%)
Statistical	0.5−4.0
Energy calibration	2.0−3.0
Beam polarization	1.0
Solid angle determination	1.3−2.0
Choice of integration region	0.3−1.0
Normalization:	
elastic cross section	1.6
choice of reference angle	0.1−2.5
Total systematic	3.1−4.9

Summary of the experimental uncertainties is shown in Table I. Errors originating in systematical effects vary between 3.1% and 4.9%. Total uncertainty, composed of statistic and systematic errors added in quadrature, lies between 3.1% and 6.3%, depending on the configuration.

III. THEORETICAL FORMALISM AND DYNAMICAL INPUT

Here we review briefly our standard scheme of 3N continuum calculations. For a general overview on 3N scattering and specifically for our way to formulate it, we refer to Ref. [3]. The inclusion of 3NF's follows the approach described in Ref. [57]. We define an amplitude T, which fulfills the Faddeev-like equation,

$$T = tP\phi + (1 + tG_0)\, V_4^{(1)}\, (1 + P)\, \phi + tPG_0T + (1 + tG_0)\, V_4^{(1)}\, (1 + P)\, G_0\, T, \tag{4}$$

with the initial channel state ϕ composed of a deuteron and a momentum eigenstate of the projectile nucleon. The NN t operator is denoted by t, the free 3N propagator by G_0, and P is the sum of a cyclical and an anticyclical permutation of three particles. The 3N force V_4 is decomposed into a sum of three parts,

$$V_4 = V_4^{(1)} + V_4^{(2)} + V_4^{(3)}, \tag{5}$$

and each $V_4^{(i)}$ is symmetric under the exchange of the nucleons jk with $j \neq i \neq k$. In Eq. (4) only $V_4^{(i)}$ enters explicitly; the others appear via the permutations contained in P. The physical breakup amplitude U_0 is obtained from T by

$$U_0 = (1 + P)T. \tag{6}$$

tat

The Faddeev-like integral equation (4) iterated and T inserted into Eq. (6) yields the multiple-scattering series, in which each term contains some number of interactions among nucleons via 2N and 3N forces with free propagation in between. This gives a transparent insight into the reaction mechanism.

As NN forces we use the new generation, realistic NN potentials AV18 [4], CD Bonn [5,6] and Nijm I and II [7].

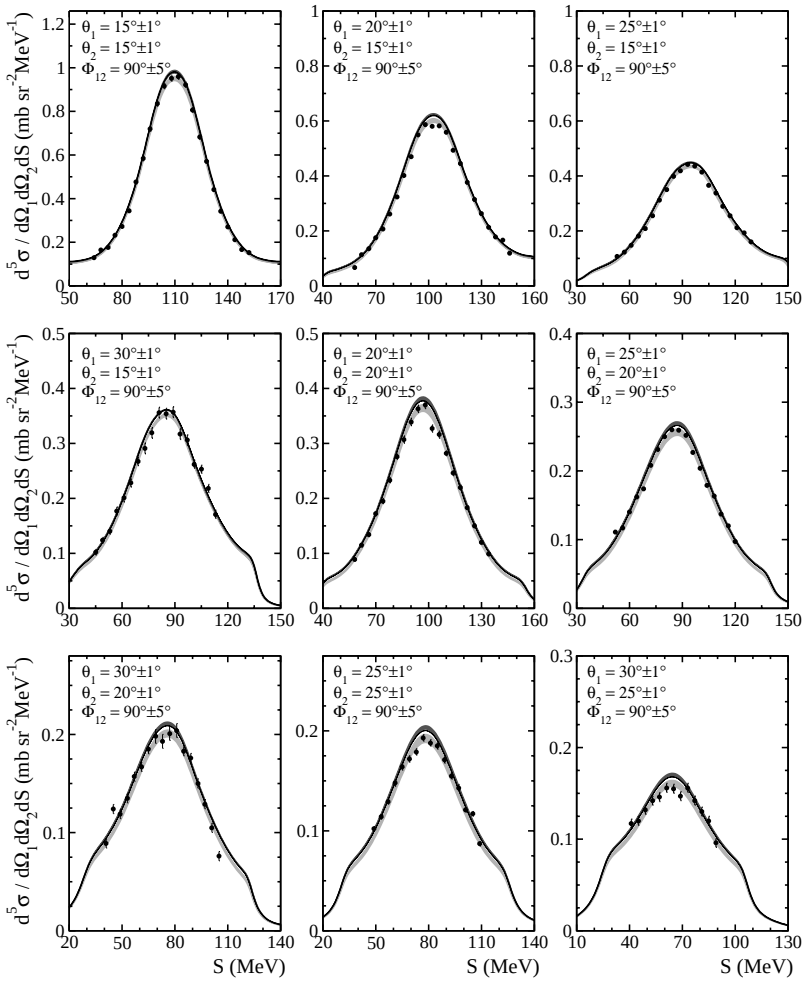

FIG. 12. Experimental breakup cross sections in nine kinematical configurations for the relative azimuthal angle ϕ_{12}=90°. The error bars represent statistical uncertainties only. The light-shaded band shows the range of theoretical predictions for cross-section values when only pairwise *NN* potentials, AV18, CD Bonn, Nijm I, and Nijm II, are used. The dark-shaded band shows the predictions when the *NN* potentials are combined with the TM99 3NF, while the solid line represents the predictions based on AV18 + Urbana IX forces combination.

We combine them with the 2π-exchange TM 3NF [32,58]. This 3NF model is based on a low momentum expansion of the π-*N* off (-the-mass-) shell scattering amplitude. The cut-off parameter Λ entering this model is used to adjust the ^{3}H binding energy for each particular *NN* and 3*N* force combination [59]. In units of the pion mass m_π, we find the Λ to be 4.856, 5.215, 5.120, and 5.072 when the TM 3NF is combined with CD Bonn, AV18, Nijm I, and Nijm II, respectively. Our adjustment of Λ is a very rough manner to take other processes into account, which can be added in a meson exchange picture. These additional processes contain different meson exchanges such as π-ρ, ρ-ρ, etc.; also different intermediate excited states might play a role [60]. To some extent such enhanced 3NF models have already been developed and applied [61–65].

The parametrization of the TM 3NF violates chiral symmetry [66,67]. A new form, consistent with chiral symmetry, which takes into account the results of Refs. [66,67], was developed in Ref. [68]. This new form will be called TM99 from now on. The corresponding Λ values (when the TM99 is used with the CD Bonn, AV18, Nijm I, and Nijm II potentials) are 4.469, 4.764, 4.690, and 4.704, respectively.

For the AV18 potential we included also the Urbana IX 3NF [31], which is based on the Fujita-Miyazawa ansatz [30] of an intermediate Δ occurring in the two-pion exchange and augmented by a spin and isospin independent short range part. The momentum space transformation of the Urbana IX 3NF has been performed in Ref. [43].

We solve Eq. (4) using a momentum space partial wave basis [3]. At the energy of the incoming deuterons, E_d^{lab} =130 MeV (equivalent to the laboratory energy of an incoming proton E_p^{lab}=65 MeV), it is necessary to take a sufficient number of partial waves into account to guarantee converged solutions of the Faddeev equations. In all presented calculations we went up to the total angular momentum j_{max}=5 in the two-nucleon subsystem. This corresponds to a maximal number of 142 partial wave states in the 3*N* system for each total 3*N* angular momentum *J*. We checked that the convergence has been achieved by looking at the results obtained for j_{max}=6 calculations without a 3NF, that increases the number of channels to 194. The inclusion of 3NF's has been carried through for all total angular momenta of the 3*N* system up to *J*=13/2. The longer range 2*N* interactions require states up to *J*=25/2 in order to get converged results. Up to now we cannot include the *pp* Coulomb force effects. We expect that at the rather high energy considered here these effects should be small.

IV. RESULTS

The analysis described in Sec. II B allows us to extract cross section for any (within the angular range of our detec-

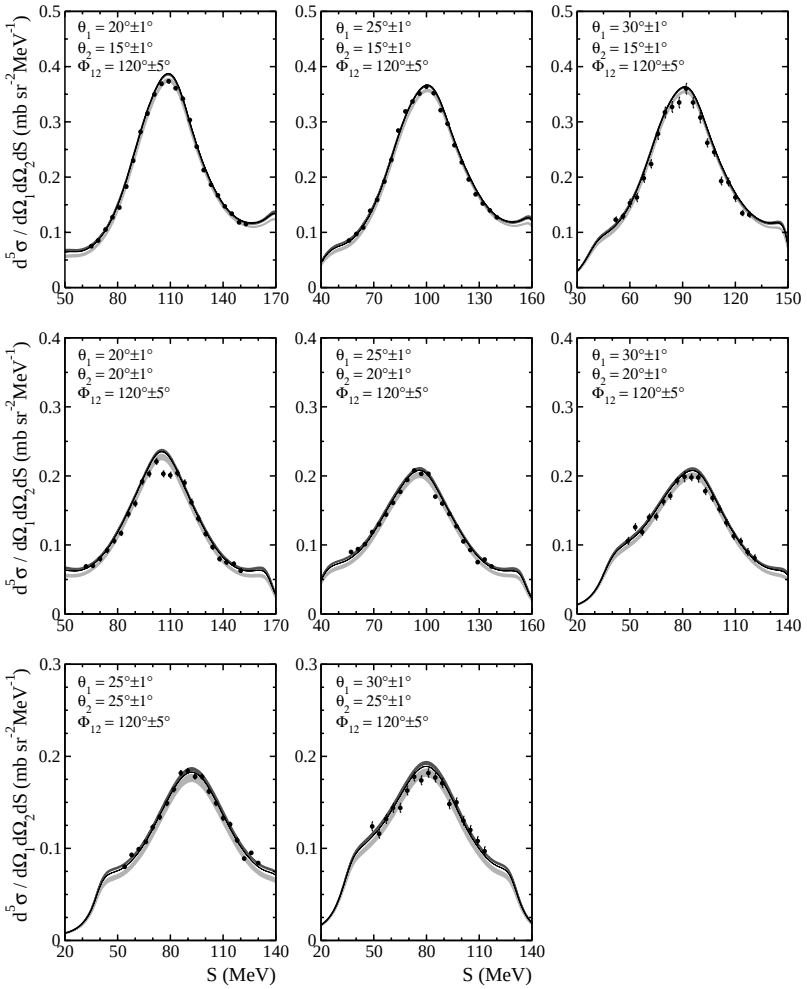

FIG. 13. The same as in Fig. 12 but in eight kinematical configurations for the relative azimuthal angle ϕ_{12}=120°.

tion system) chosen configuration of the breakup reaction. In this paper we concentrate on configurations, in which the cross section values are relatively large, despite the fact that these are usually not the ones, in which the predicted 3NF effects are the largest.

The cross-section data in 38 kinematically complete configurations described by angles of the two registered protons (θ_1, θ_2, and ϕ_{12}), are presented in Figs. 12–16 as a function of the arc-length S along the kinematical curve. For each geometry the values of θ_1, θ_2, and ϕ_{12} are indicated in the corresponding panel. To reach sufficient statistical accuracy while keeping the angular and energy integrating effects to a minimum, the data have been averaged over the ranges of the polar angles of $\Delta\theta_1=\Delta\theta_2=2°$, the azimuthal angle of $\Delta\phi_{12}=10°$, and the arclength of $\Delta S=4$ MeV around the central values of θ_1, θ_2, ϕ_{12}, and S, defining each data point. Error bars shown in Figs. 12–16 correspond to statistical uncertainties only.

The experimental cross sections have been compared to theoretical predictions based on the solutions of the 3N Faddeev equations with the AV18, CD Bonn, Nijm I, and Nijm II potential only (light-shaded bands in Figs. 12–16) and their combinations with the 2π-exchange TM and TM99 3NF's. Since in most cases the predictions for various *NN* potentials combined with the TM and TM99 3NF's strongly overlap, for clarity in Figs. 12–16 only the results obtained with those four *NN* forces combined with the TM99 3NF are shown as dark-shaded bands. In addition, the cross sections have been compared to the predictions of the AV18 potential combined with the Urbana IX 3NF (solid lines in Figs. 12–16).

In view of the averaging inherently present in the data, the point-geometry theoretical predictions should be averaged over the finite angular and energy resolutions of the experiment. This averaging problem was studied in detail in our analysis of the *pd* breakup reaction at an incoming proton energy E_p^{lab}=65 MeV [46]. It was found that the resulting modifications of the cross sections have been negligible in most breakup configurations. Calculations performed for the present experimental conditions showed very small (below 1.5%, depending on configuration) mean differences between the point-geometry and averaged predictions, when considering the ranges of S values covered by the experimental data. For all considered configurations the averaging leads to an enhancement of the cross-section values, in a way practically equivalent to multiplying of the distribution (within the relevant S range) by a small constant factor. It has been found that this behavior is very similar for averaging the predictions obtained with *NN* potentials only and including also 3NF's. Such an effect can be considered as equivalent to a small change of the experimental normalization factor. In view of these results and having in mind additional tests, which eliminate the influence of the data normalization on

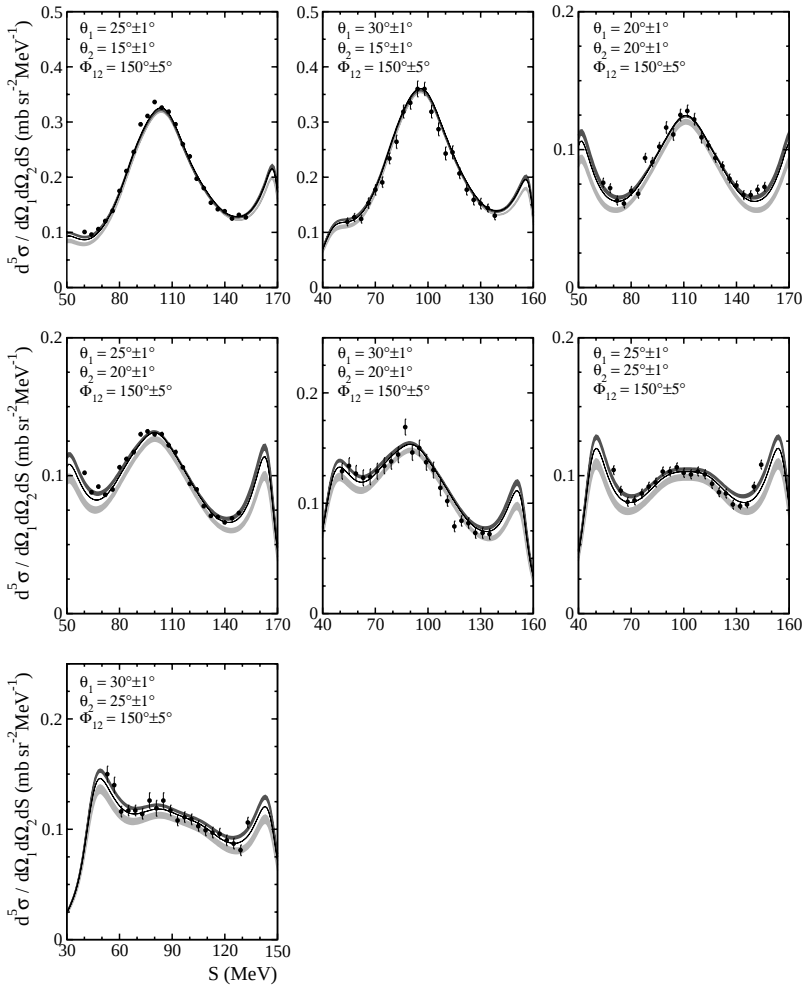

FIG. 14. The same as in Fig. 12 but in 7 kinematical configurations for the relative azimuthal angle ϕ_{12}=150°.

the conclusions about the 3NF effects (see further below), the experimental cross sections have been compared with the point-geometry theoretical predictions calculated at the central values of the experimental intervals of the kinematical variables.

As can be seen in Figs. 12–16 the predicted 3NF effects depend on the geometry of the outgoing protons. In some configurations their effects are distributed nearly uniformly along the *S* curve, while in others they are located at specific regions of *S*. Practically, in all cases the inclusion of the 3NF increases the cross section. In some configurations, especially in those characterized by a small value of the relative azimuthal angle ϕ_{12} (Figs. 12 and 13), the 3NF effects are relatively small. For these configurations a nice agreement between the data and theory is found. In geometries, for which the predicted 3NF effects are relatively larger, the quality of the description of the data generally seems to improve when the 3NF is included. It can also be observed that the increase of the cross-section values when the 3NF is included is larger for the TM99 combined with any of the four used *NN* potentials than for the AV18+Urbana IX combination.

Taking as an example the CD Bonn potential predictions, one observes that in 23 out of 38 presented configurations the inclusion of the TM 3NF improves the agreement between the data and the theory. This improvement is clearly seen in decreased values of χ^2 per degree of freedom obtained for each of these configurations. In the other 15 kinematical configurations data seem to prefer the predictions based on the CD Bonn potential alone. Similar conclusions are observed for other combinations of *NN* and 3*N* forces. Since no striking systematic pattern can be observed for any choice of $\theta_1,\theta_2,\phi_{12}$, or their combinations, we performed a global comparison, based on the values of χ^2 per degree of freedom for all 38 configurations taken together, to resolve the question whether the inclusion of the 3NF improves or deteriorates the cross-section data description. In this way we can compare numbers, characterizing the quality of the description of the cross-section data by one of the two sets of theoretical predictions: χ^2_{2N} for predictions based on pairwise *NN* potentials only and χ^2_{2N+3N} for the cases where a 3NF was included in the calculations. Comparing these numbers, shown in the second column of Table II, one can conclude that including any of the 3NF's applied in this study improves the description of our data. For the four *NN* forces used, this improvement in χ^2 per degree of freedom varies between about 10% and 50%. It should be noted that the deviations of the χ^2 values from 1 are not astonishing since the overall normalization error is here not included in the experimental uncertainties.

Since the most relevant systematical factor influencing the magnitude of the experimental cross sections is their abso-

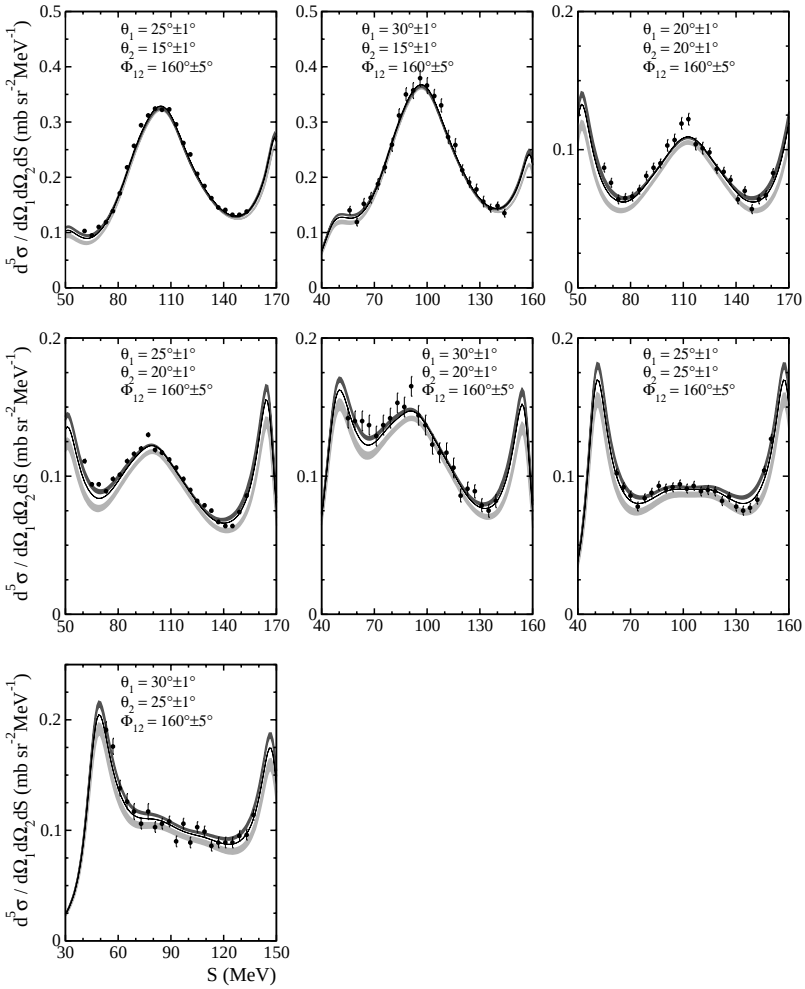

FIG. 15. The same as in Fig. 12 but in seven kinematical configurations for the relative azimuthal angle ϕ_{12}=160°.

lute normalization, it seems to be worthwhile to study the agreement between the data and the two chosen sets of the theoretical predictions (with and without 3NF), when the experimental cross-section normalization is allowed to be slightly changed. In such an approach one puts more weight on the shapes of the measured distributions, rather than on their absolute normalization, as obtained in the course of the data analysis (cf. Sec. II B).

Applying different normalization factors when comparing the data with calculations based on 2*N* dynamics only and on predictions with a 3NF included, allows us to avoid possible false conclusions about which set of theoretical predictions better reproduces the data. As previously mentioned, in practically all our configurations the inclusion of 3NF's increases the absolute value of the predicted cross section. Thus, having experimentally determined, e.g., slightly too large normalization factor, might easily result in shifting the data from the results of the calculation, with only *NN* potential towards better agreement with the predictions including also a 3NF. Then, trusting only the experimental normalization, without performing below described tests, would result in an erroneous statement. Since, however, the *shapes* of both sets of theoretical prediction differ, by allowing the normalization to be varied, we can resolve the question which calculations reproduce the data better, since the relative normalization of the data points in a given configuration is determined exactly. By employing this method we also eliminate the small influence of averaging, present inherently in the data and omitted in the theoretical predictions (averaging does not change the shape of the cross-section distribution).

To achieve this purpose we applied an extra normalization factor λ to the data, common for all 38 configurations, and varied it by about ±10% around λ=1. This floating of the data was allowed in relation to both sets of the theoretical predictions, separately for all four *NN* potentials, without and with the 3NF, and the χ^2 analysis was redone for each considered combination of forces. The results are illustrated for the case of the CD Bonn potential and its combination with the TM 3NF in Fig. 17. This example demonstrates that the χ^2_{2N} and χ^2_{2N+3N} as functions of λ reveal well-defined minima, occurring for those particular forces at the normalization factors λ=0.985 and λ=1.020, respectively. When using these values for all configurations discussed, in 29 out of 38 cases the data show better agreement with the predictions including the 3NF effects. Analogous procedures performed for the other *NN* potentials and their combinations with 3NF's lead to χ^2 minima for the values of the λ factor between 0.96 and 1.03. It should be noted that these values of λ lie well within the quoted normalization uncertainty. The values of χ^2 per degree of freedom obtained at the corresponding minima are shown in the third column of Table II. They again support the preference of the dynamics containing 3NF's in describ-

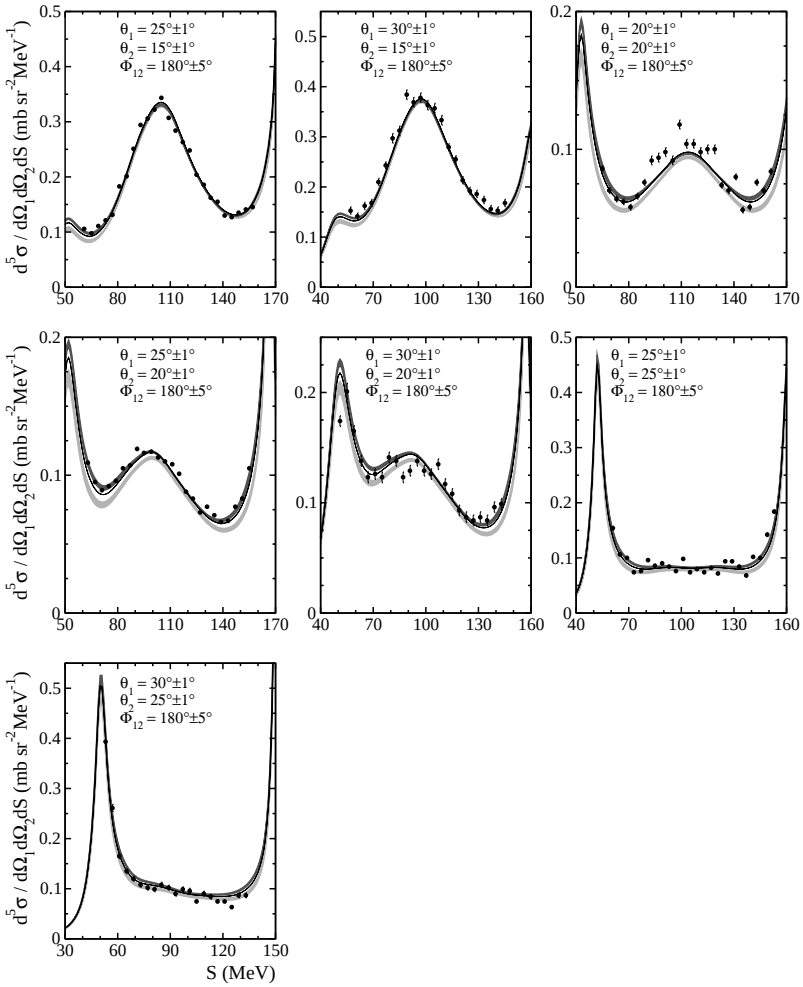

FIG. 16. The same as in Fig. 12 but at seven kinematical configurations for the relative azimuthal angle ϕ_{12}=180°.

ing our experimental cross sections, as shown by the improvement of the χ^2 value by 20–40 %, depending on the *NN* potential considered.

To extend this investigation even further, we have applied individual normalization factors λ for each of our 38 kinematical configurations and each combination of forces considered. In each configuration, the experimental cross-section data were separately normalized to fit best either the calculations based on a pairwise *NN* potential alone or the predictions with a 3NF included. For the chosen example case of the CD Bonn and CD Bonn+TM+3NF based predictions, after such an individual renormalization the agreement is better in 32 out of 38 configurations when the TM 3NF is included in the calculations. Again, for all investigated combinations of forces, after finding the individual best normalization factors, the total χ^2 per degree of freedom were calculated for all configurations. The resulting values are shown in the fourth column of Table II. In this approach only the shapes of the experimental and theoretical cross-section distributions are compared, neglecting totally the absolute experimental normalization. Again a preference of the theoretical predictions with 3NF's by our data was found, leading to a reduction of the total χ^2 value per degree of freedom by 20–40 %, when a 3NF was taken into account. Also in these procedures the obtained values of the renormalization factor λ were not far from the nominal value, ranging between 0.92 and 1.07.

Regarding again Figs. 12–16, one notices that there are several breakup configurations where the inclusion of 3NF forces leads to predictions deviating significantly from the ones based on *NN* forces only and where high-precision data would be especially rewarding. Apparently, these can be found in Figs. 14 and 15. As mentioned in the Introduction, there are also other configurations, where present day nuclear force models predict even larger effects [48,50]. In the next stage of the data analysis, with higher statistics of data available, those configurations will be investigated as well. It is also worthwhile to consider dedicated measurements focused on such configurations and performed with a few isolated detectors, thus gaining selectively even higher statistics.

V. SUMMARY AND CONCLUSIONS

The measurement of the deuteron-proton ^{1}H(*d*,*pp*)*n* breakup cross sections using a 130 MeV deuteron beam was performed in a large part of the available phase space. In this paper high-precision, fivefold differential cross-section data for 38 kinematically complete configurations at different angular combinations of the two outgoing protons are presented.

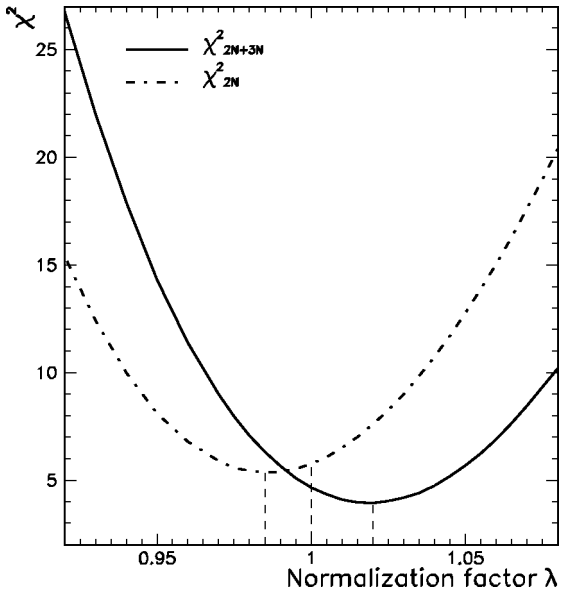

FIG. 17. Example of the dependence of the χ^2 per degree of freedom on the normalization factor λ, by which the experimental cross sections in all configurations have been multiplied. The dash-dotted line (χ^2_{2N}) refers to the theoretical predictions with the CD Bonn potential only, while the solid line (χ^2_{2N+3N}) corresponds to the theory with the TM 3NF included.

TABLE II. Agreement between the experimental cross sections and the theoretical predictions implementing different *NN* potentials: AV18, CD Bonn, Nijm I, Nijm II (χ^2_{2N}), and their combinations with various 3NF models: TM, TM99, and Urbana IX (χ^2_{2N+3N}). In the three columns the quality of agreement between data and theory, as given by the χ^2 value per degree of freedom, is shown for different treatments of the experimental data normalization, as explained in the text.

2*N* and 3*N* forces	Normalization		
	Experimental	Global fit	Individual fit
		χ^2_{2N}	
AV18	9.5	6.4	4.3
CD Bonn	5.7	5.4	3.6
Nijm I	7.1	5.9	4.3
Nijm II	8.1	6.3	3.9
		χ^2_{2N+3N}	
AV18+TM	4.4	3.6	2.9
CD Bonn+TM	4.7	3.9	2.8
Nijm I+TM	5.4	3.9	3.1
Nijm II+TM	5.2	3.8	3.0
AV18+TM99	4.6	3.7	2.7
CD Bonn+TM99	5.2	4.3	2.7
Nijm I+TM99	5.8	4.1	2.7
Nijm II+TM99	5.5	3.9	2.7
AV18+Urbanna IX	4.6	4.2	2.9

We compared these cross sections to theoretical predictions based on the realistic *NN* potentials AV18, CD Bonn, Nijm I, and Nijm II only and to those obtained when, in addition, the TM or TM99 3NF model was included in the 3*N* Hamiltonian. For AV18 also the Urbana IX 3NF was used for calculating the theoretical cross sections. The magnitude of the predicted 3NF effects generally depends on the configuration. In some studied final state geometries these effects are practically negligible and in such cases the cross-section data are in a very good agreement with the theoretical predictions.

In the majority of the analyzed configurations the effects of the 3NF are not negligible. In general, the inclusion of a 3NF in the calculations leads to an increase of the cross-section value. This effect is less pronounced for combining the Urbana IX 3NF with the AV18 *NN* potential than for the TM and TM99 forces combined with any of the four *NN* potentials used. The inclusion of the TM and TM99 3NF forces leads to quite similar results in all studied configurations. The agreement between the experimental cross sections and theoretical predictions generally improves when a 3NF is taken into account. This conclusion is valid for all combinations of any of the four *NN* potentials used with the TM or TM99 (in case of AV18 also with Urbana IX) 3NF. It is strongly supported by a procedure, in which a slight floating of the normalization of the data (within the experimental systematic error) is allowed. With such treatments of the experimental data normalization, their agreement with the theory including 3NF's is even improved.

Our present study clearly shows a significant influence of 3NF's on the breakup cross sections at the energy of our measurement. It demonstrates the usefulness of the breakup reaction as a tool to study the nuclear Hamiltonian. With more configurations analyzed, polarization observables added to the cross-section results, and higher statistics provided, it will probably become possible to make a stronger conclusion on the quality of the present 3NF models.

In order to fully understand the Nd scattering dynamics at higher energies, it is necessary, in addition to the inclusion of 3NF's, to formulate the equations in a relativistically invariant way. Also the exact inclusion of the *pp* Coulomb force in the *pd* scattering at energies above the deuteron breakup threshold is still unsolved and leaves a very uncomfortable theoretical uncertainty in the analysis of the *pd* data. The solution of these two problems will remove the remaining uncertainties and will make Nd scattering an extremely precise tool for testing nuclear interactions. It will also allow the computation of exact 3*N* wave functions that can be applied to study electromagnetic processes in the 3*N* system in a wide range of energies, as well as to provide some basis for exact calculations in many-body systems.

ACKNOWLEDGMENTS

This work was supported by the Polish Committee for Scientific Research under Grant No. 2P03B02818 and the NSF under Grant No. PHY0070858. One of the authors (R.S.) acknowledges financial support of the Foundation for Polish Science. The numerical calculations have been performed on the Cray T90 and T3E of the NIC in Jülich, Germany.

[1] W. Meier and W. Glöckle, Phys. Lett. **138B**, 329 (1984); B. H. J. McKeller and W. Glöckle, Nucl. Phys. **A416**, 435 (1984).
[2] B. F. Gibson, in *Proceedings of the International Symposium on the Three-Body Force in the Three-Nucleon System, Washington, D.C. 1986,* edited by B. L. Berman and B. F. Gibson [Lecture Notes in Physics **260**, 511 (1986)].
[3] W. Glöckle, H. Witała, D. Hüber, H. Kamada, and J. Golak, Phys. Rep. **274**, 107 (1996).
[4] R. B. Wiringa, V. G. J. Stoks, and R. Schiavilla, Phys. Rev. C **51**, 38 (1995).
[5] R. Machleidt, F. Sammarruca, and Y. Song, Phys. Rev. C **53**, R1483 (1996).
[6] R. Machleidt, Phys. Rev. C **63**, 024001 (2001).
[7] V. G. J. Stoks, R. A. M. Klomp, C. P. F. Terheggen, and J. J. de Swart, Phys. Rev. C **49**, 2950 (1994).
[8] S. Weinberg, Phys. Lett. B **251**, 288 (1990); Nucl. Phys. **B363**, 3 (1991).
[9] U. van Kolck, Phys. Rev. C **49**, 2932 (1994).
[10] C. Ordoñez, L. Ray, and U. van Kolck, Phys. Rev. C **53**, 2086 (1996).
[11] T.-S. Park, K. Kubodera, D.-P. Min, and M. Rho, Nucl. Phys. **A646**, 83 (1999).
[12] N. Kaiser, R. Brockmann, and W. Weise, Nucl. Phys. **A625**, 758 (1997).
[13] N. Kaiser, S. Gerstendörfer, and W. Weise, Nucl. Phys. **A637**, 395 (1998).
[14] E. Epelbaum, W. Glöckle, and U.-G. Meißner, Nucl. Phys. **A637**, 107 (1998).
[15] E. Epelbaum, W. Glöckle, and U.-G. Meißner, Nucl. Phys. **A671**, 295 (2000).
[16] E. Epelbaum, H. Kamada, A. Nogga, H. Witała, W. Glöckle, and U.-G. Meißner, Phys. Rev. Lett. **86**, 4787 (2001).
[17] D. R. Entem and R. Machleidt, Phys. Rev. C **66**, 014002 (2002).
[18] D. R. Entem and R. Machleidt, nucl-th/0304018.
[19] E. Epelbaum, A. Nogga, W. Glöckle, H. Kamada, U.-G. Meissner, and H. Witała, Eur. Phys. J. A **15**, 543 (2002).
[20] E. Epelbaum, A. Nogga, W. Glöckle, H. Kamada, U.-G. Meissner, and H. Witała, Phys. Rev. C **66**, 064001 (2002).
[21] D. R. Entem, R. Machleidt, and H. Witała, Phys. Rev. C **65**, 064005 (2002).
[22] A. Nogga, H. Kamada, and W. Glöckle, Phys. Rev. Lett. **85**, 944 (2000).
[23] M. Viviani, Nucl. Phys. **A631**, 111c (1998).
[24] A. Nogga, H. Kamada, W. Glöckle, and B. R. Barrett, Phys. Rev. C **65**, 054003 (2002).
[25] J. Carlson and R. Schiavilla, Rev. Mod. Phys. **70**, 743 (1998).
[26] R. B. Wiringa, S. C. Pieper, J. Carlson, and V. R. Pandharipande, Phys. Rev. C **62**, 014001 (2000).
[27] S. C. Pieper and R. B. Wiringa, Annu. Rev. Nucl. Part. Sci. **51**, 53 (2001).
[28] E. Caurier, P. Navratil, W. E. Ormand, and J. P. Vary, Phys. Rev. C **66**, 024314 (2002).
[29] S. C. Pieper, K. Varga, and R. B. Wiringa, Phys. Rev. C **66**, 044310 (2002).
[30] J. Fujita and H. Miyazawa, Prog. Theor. Phys. **17**, 360 (1957).
[31] B. S. Pudliner, V. R. Pandharipande, J. Carlson, S. C. Pieper, and R. B. Wiringa, Phys. Rev. C **56**, 1720 (1997).
[32] S. A. Coon *et al.*, Nucl. Phys. **A317**, 242 (1979).
[33] S. C. Pieper *et al.*, Phys. Rev. C **64**, 014001 (2001).
[34] H. Sakai *et al.*, Phys. Rev. Lett. **84**, 5288 (2000).
[35] N. Sakamoto *et al.*, Phys. Lett. B **367**, 60 (1996).
[36] W. Tornow, C. R. Howell, R. C. Byrd, R. S. Pedroni, and R. L. Walter, Phys. Rev. Lett. **49**, 312 (1982).
[37] R. V. Cadman *et al.*, Phys. Rev. Lett. **86**, 967 (2001).
[38] R. Bieber *et al.*, Phys. Rev. Lett. **84**, 606 (2000).
[39] K. Ermisch *et al.*, Phys. Rev. Lett. **86**, 5862 (2001).
[40] P. Hempen *et al.*, Phys. Rev. C **57**, 484 (1998).
[41] W. Grüebler, Nucl. Phys. **A353**, 31c (1981).
[42] L. Sydow *et al.*, Nucl. Phys. **A567**, 55 (1994); Few-Body Syst. **25**, 133 (1998).
[43] H. Witała, W. Glöckle, J. Golak, A. Nogga, H. Kamada, R. Skibiński, and J. Kuroś-Żołnierczuk, Phys. Rev. C **63**, 024007 (2001).
[44] K. Sekiguchi *et al.*, Phys. Rev. C **65**, 034003 (2002).
[45] M. Allet *et al.*, Phys. Lett. B **376**, 255 (1996).
[46] J. Zejma *et al.*, Phys. Rev. C **55**, 42 (1997).
[47] K. Bodek *et al.*, Few-Body Syst. **30**, 65 (2001).
[48] J. Kuroś-Żołnierczuk, Ph.D. thesis, Jagellonian University, 2001.
[49] J. Kuroś-Żołnierczuk, H. Witała, J. Golak, H. Kamada, A. Nogga, R. Skibiński, and W. Glöckle, Phys. Rev. C **66**, 024003 (2002).
[50] J. Kuroś-Żołnierczuk, H. Witała, J. Golak, H. Kamada, A. Nogga, R. Skibiński, and W. Glöckle, Phys. Rev. C **66**, 024004 (2002).
[51] N. Kalantar-Nayestanaki, J. Mulder, and J. Zijlstra, Nucl. Instrum. Methods Phys. Res. A **417**, 215 (1998).
[52] N. Kalantar-Nayestanaki *et al.*, Nucl. Instrum. Methods Phys. Res. A **444**, 591 (2000).
[53] M. Volkerts, A. Bakker, N. Kalantar-Nayestanaki, H. Fraiquin, A. Eads, T. Rinckel, and K. Solberg, Nucl. Instrum. Methods Phys. Res. A **428**, 432 (1999)
[54] S. Schaddmand, J. C. S. Bacelar, H. A. P. van der Duin, N. Kalantar-Nayestanaki, and H. W. Wilschut, Nucl. Instrum. Methods Phys. Res. A **423**, 174 (1999).
[55] A. Micherdzińska, Ph.D. thesis, University of Silesia, 2003.
[56] H. Shimizu, K. Imai, N. Tamura, K. Nisimura, K. Hatanaka, T. Saito, Y. Koike, and Y. Taniguchi, Nucl. Phys. **A382**, 242 (1982).
[57] D. Hüber, H. Kamada, H. Witała, and W. Glöckle, Acta Phys. Pol. B **28**, 1677 (1997).
[58] S. A. Coon and W. Glöckle, Phys. Rev. C **23**, 1790 (1981).
[59] A. Nogga, D. Hüber, H. Kamada, and W. Glöckle, Phys. Lett. B **409**, 19 (1997).
[60] For a short review, see M. R. Robilotta, Few-Body Syst., Suppl. **2**, 35 (1987).
[61] S. A. Coon and M. T. Peña, Phys. Rev. C **48**, 2559 (1993).
[62] S. A. Coon, M. T. Peña, and D. O. Riska, Phys. Rev. C **52**, 2925 (1995).
[63] B. D. Keister and R. B. Wiringa, Phys. Lett. B **173**, 5 (1986).
[64] T.-Y. Saito and J. Haidenbauer, Eur. Phys. J. A **7**, 559 (2000).
[65] H. Witała *et al.*, Phys. Rev. C **52**, 1254 (1995).
[66] J. L. Friar, D. Hüber, and U. van Kolck, Phys. Rev. C **59**, 53 (1999).
[67] D. Hüber, J. L. Friar, A. Nogga, H. Witała, and U. van Kolck, Few-Body Syst. **30**, 95 (2001).
[68] S. A. Coon and H. K. Han, Few-Body Syst. **30**, 131 (2001).